Iron oxide-carbon core-shell nanoparticles for dual-modal imaging-guided photothermal therapy

Hui Wang[a,b], **Qingxin Mu**[a], **Richard Revia**[a], **Kui Wang**[a], **Bowei Tian**[d], **Guanyou Lin**[a], **Woncheol Lee**[c], **Yang-Ki Hong**[c], and **Miqin Zhang**[a]

[a]Department of Materials Science and Engineering University of Washington, Seattle, WA 98195, USA

[b]High Magnetic Field Laboratory, Hefei Institutes of Physical Science, Chinese Academy of Sciences, Hefei, AH, 230031, China

[c]Department of Electrical and Computer Engineering and MINT Center, The University of Alabama, Tuscaloosa, AL 35487, USA

[d]Department of Applied Mathematics, University of Washington, Seattle, WA 98195, USA

Abstract

Nanostructured materials that have low tissue toxicity, multi-modal imaging capability and high photothermal conversion efficiency have great potential to enable image-guided near infrared (NIR) photothermal therapy (PTT). Here, we report a bifunctional nanoparticle (BFNP, ~16 nm) comprised of a magnetic Fe_3O_4 core (~9.1 nm) covered by a fluorescent carbon shell (~3.4 nm) and prepared via a one-pot solvothermal synthesis method using ferrocene as the sole source. The BFNP exhibits excitation wavelength-tunable, upconverted and near-infrared (NIR) fluorescence property due to the presence of the carbon shell, and superparamagnetic behavior resulted from the Fe_3O_4 core. BFNPs demonstrate dual-modal imaging capacity both in vitro and in vivo with fluorescent imaging excited under a varying wavelength from 405 nm to 820 nm and with T_2-weighted magnetic resonance imaging ($r_2 = 264.76$ mM^{-1} s^{-1}). More significantly, BFNPs absorb and convert NIR light to heat enabling photothermal therapy as demonstrated mice bearing C6 glioblastoma. These BFNPs show promise as an advanced nanoplatform to provide imaging guided photothermal therapy.

Keywords

hybrid nanoparticles; carbon shell; magnetic core; multi-modal imaging; photothermal therapy

---

Correspondence to: Miqin Zhang.

1. Introduction

Photothermal therapy (PTT) is a cancer treatment recourse whose efficacy primarily depends on the ability of the deployed phototherapeutic agents to absorb electromagnetic radiation from a known source and convert it into localized heat [1, 2], The current standard of cancer remediation typically involves surgical resection, which does not always result in the utter removal of cancerous tissue, followed by the administration of chemotherapeutics and radiation therapy, which are both toxic to healthy tissues. In contrast to the nonselective cellular destruction attendant to chemotherapy and radiotherapy, PTT capitalizes on the human body's translucency to near-infrared (NIR) light allowing a laser to penetrate deep into tissues noninvasively and energize phototherapeutic agents exposed to photons to increase the temperature in their vicinity to above a threshold at which cell death occurs [3, 4], Thermal ablation of healthy tissue is thus minimized in PTT by spatially controlling the NIR light source to illuminate only pre-defined regions. Spatial regulation of NIR exposure paired with the ability of prudently designed phototherapeutics to passively and actively target cancerous lesions discriminately over normal tissue reinforces PTT with another layer of specificity that chemotherapy and radiotherapy lack. To bring PTT out of the realm of the laboratory and into the clinic, phototherapeutic agents with the following properties must be made available: high photothermal energy conversion efficiency, low tissue toxicity, and tumor-targeting capability [4, 5], Additionally, it would be highly advantageous to be able to monitor the location, distribution profile, and retention and secretion properties of phototherapeutics over the course of the therapy with an noninvasive imaging technique such as fluorescence (FL) or magnetic resonance imaging (MRI) [6–8]. The combination of phototherapeutic and imaging capabilities in a single particle would allow for the precise identification of tumor regions and verification that phototherapeutics are within cancer lesions during the treatment process of PTT [9–13].

A number of materials have been investigated as phototherapeutic agents for PTT including gold nanoparticles [14, 15], copper sulfide nanocrystals (CuS) [16], molybdenum sulfide nanosheets (MoS_2) [17, 18], carbon materials [19–22], conjugated polymers [23], metal-organic frameworks [13], and iron oxide nanoparticles [24, 25]. Many of these thermo-optically active nanomaterials demonstrated to be highly effective in ablating cancer in preclinical animal models [26, 27]. However, most of the reported phototherapeutic agents serve only as photon absorbers that convert light into heat without imaging capability, or vice versa, or they are toxic to cells and tissues in nature limiting their application in medicine.[23, 28, 29] A low tissue toxic phototherapeutic agent coupled with an imaging capacity such as MRI or an FL imaging or both would be highly desirable in clinical settings. MRI is a pervasive imaging modality used in cancer detection because of its high-spatial resolution and safe profile [30]. In order to accurately distinguish lesions from healthy tissues, MRI contrast agents are commonly employed [31, 32]. In FL imaging, an exogenous light source is used to excite fluorophores residing in regions of interest being imaged. These fluorophores absorb energy from the light source and in response emit photons of a different wavelength than the source photons. FL imaging has been used in image-guided surgery wherein fluorescent probes aid surgeons to better view the boundaries of malignant tissues being removed [33].

Here, we report on the development of a bifunctional nanoparticle (BFNP) formulation that demonstrates efficient photothermal energy conversion for PTT while providing contrast enhancement for both MRI and fluorescence imaging. The BFNP is comprised of an FesCV core and a carbon shell, with an average diameter of approximately 16 nm, which is considerably smaller than all the Fe_3O_4 cluster/carbon core/shell NPs reported thus far (>100 nm) and is highly desirable for vivo application [34], BFNPs are synthesized by a simple one-pot high-yield process. These BFNPs demonstrate photoluminescence property and have thus the potential to serve as a detectable optical marker in FL imaging. Similarly, the superparamagnetic iron oxide cores of BFNPs provide a source of T_2 contrast enhancement in T_2-weighted MRI. In vitro experiments and in vivo experiments were performed to test their cytotoxicity and tissue toxicity, respectively. Finally, BFNPs are tested for their ability to kill tumor cells in vitro and inhibit tumor growth in vivo via photothermal therapy.

2. Experimental section

2.1. Synthesis of BFNPs

Ferrocene (0.01 g, Aldrich) was dissolved in acetone (30 mL, Aldrich) in a 50 mL beaker covered with a foil to avoid the volatilization of acetone. After intense sonication (42 kHz, EW-08891-21 sonicator, Cole-Parmer) for 30 min at room temperature, 1.0 mL of 30% H_2O_2 (Aldrich) solution was slowly added using a pipette within 30 min while stirring. The resultant mixture solution was further stirred for 30 min with a magnetic stirring apparatus. This precursor solution was transferred to a 50.0 mL Teflon-lined stainless-steel autoclave. After sealing, the autoclave was heated to and maintained at 200°C for 24 h. The autoclave was then cooled naturally to room temperature. After intense sonication for 15 min, the brown solution from the autoclave were magnetized for 10 min with a rare earth neodymium magnet (model N52, 2 cm × 2 cm × 1 cm). The resultant BFNPs were adsorbed to the bottom of a beaker (50 mL) and the supernatant was discarded under the applied magnetic field. BFNPs were then washed with acetone three times to remove carbon-based by-products. Finally, BFNPs were cool-dried in a vacuum oven.

2.2. Characterization

TEM and high-resolution TEM images were acquired on a Tecnai G2 F20 electron microscope (FEI, Hillsboro, OR) operating at a voltage of 200 kV. Powder X-ray diffraction (XRD) patterns were acquired from lyophilized samples using a D8 Bruker X-ray diffractometer with Cu Kα radiation. Raman spectra were acquired with a Raman-Microscope (Renishaw-InVia) using an Ar$^+$ laser (514.5 nm) at room temperature. UV-Vis absorption spectra were obtained on a UV-Vis Spectrometer (Agilent Technologies, Santa Clara, CA). PL spectra were obtained on a JOBIN YVON Co. FluoroMax®–3 Spectrofluorometer equipped with a Hamamatsu R928P photomultiplier tube. X-ray photoelectron spectroscopy (XPS) experiments were carried out at the National ESCA and Surface Analysis Center. The magnetic properties of BFNPs were measured using a superconducting quantum interference device magnetometer (Quantum Design MPMS XL-7). The hydrodynamic size was determined using a Zetasizer Nano-ZS (Malvern Instruments, Worcestershire, UK) at room temperature. Fourier transform infrared (FT-IR)

spectra were acquired using a Nicolet 5-DXB FTIR spectrometer with a resolution of 4 cm^{-1}.

2.3. Cell culture

Human SF-763 glioblastoma cells were kindly provided by Prof John R. Silber and grown in Dulbecco's Modified Eagle's Medium (DMEM) supplemented with 10% fetal bovine serum and 1% antibiotic-antimycotic (Life technologies, Grand Island, NY). Cells were cultured in an incubator maintained at 37°C and 5% CO_2 with 95% humidity.

2.4 In vitro confocal imaging

SF-763 cells were seeded onto glass cover slips in a 6-well plate. After overnight incubation, cells were incubated with BFNPs (50 μg/mL) for 2 h. Cells were then washed with cold PBS 3 times and fixed with 4% paraformaldehyde for 15 min at 37°C. Cells were then mounted onto glass slides with ProLong® Gold Antifade Mountant (Life Technologies Inc., Gaithersburg, MD). The images of cells were acquired using a Laser Scanning Microscope Leica SP8X (Leica Microsystems GmbH, Germany). Three excitation wavelengths were used: 405, 488 and 546 nm.

2.5 In vitro two-photon fluorescent imaging

SF-763 cells were seeded onto glass cover slips in a 24-well plate. Twenty-four hours after seeding, cells were incubated with BFNPs (50 μg/mL) for 2 h. Cells were then washed with PBS 3× and fixed with 4% paraformaldehyde for 10 min. Nuclei were stained with DAPI before cells were mounted onto glass slides with ProLong® Gold Antifade Mountant (Life Technologies Inc., Gaithersburg, MD). Two-photon imaging was performed using an Olympus FV1000 MPE BX61 multi-photon microscope with excitation wavelength of 820 nm.

2.6 In vivo NIR imaging

All animal studies were conducted in accordance with the University of Washington's Institute of Animal Care and Use Committee (IACUC) approved protocols as well as with federal guidelines. BFNPs were injected intratumorally into athymic nude mice (Jackson Labs, Bar Harbor, ME). Fluorescence images were taken with a Xenogen IVIS imaging system (PerkinElmer Inc.).

2.7 In vitro MRI

MRI measurements were conducted on a Bruker Avance III 600 MHz, 14 T wide bore spectrometer. BFNPs in phosphate buffered saline were pipetted into glass vials (3.25 mm I.D., 5 mm O.D., 200 μL volume). The vials were fixed in place inside a water reservoir; the water served as a homogeneous background signal to minimize magnetic susceptibility variations near the samples. The secured vials were placed in a 25-mm single-channel ^{1}H radiofrequency receiving coil (PB Micro 2.5). T_2 values were measured using a multi-spin multi-echo (MSME) pulse sequence with TR = 2500 ms, TE = 6.7 + 6n ms (n = 0–16), and 78×156 μm^2 in-plane resolution with 0.5 mm slice thickness for 14 slices. T_2-weighted

images were acquired with a RARE pulse sequence with TE = 6.78 ms, TR= 4000 ms, and 78×52 μm^2 in-plane resolution with 0.5 mm slice thickness for 14 slices.

2.8   In vivo MRI

T_2-weighted imaging was performed on C57BL/6 wild-type mice prior to and after BFNP injection (200 μL, 1 mg/mL), using a Bruker Avance III 600 MHz, 14 T vertical-bore imaging system. Mice were anesthetized with isoflurane (Piramal Healthcare), and fixed in a coil-integrated respiratory monitoring system (SA Instruments; MR-compatible small animal monitoring and gating system) with nose-cone for oxygen/anesthetic, ear-bar head holder, circulating-bath temperature control, respiratory monitoring, and residual gas extraction. Abdominal scans were performed using rapid acquisition with refocused echoes (RARE) T_2-weighted (TR/TE = 691/5.5 ms, in-plane resolution 93×62 μm^2, matrix 256×284) sequence with slices placed in the transverse plane with 0.5 mm slice thickness and 0.75 mm interslice gap allowing for coverage from the liver to the pelvic floor.

2.9   Cell viability

SF-763 and HEK293T cells were seeded in a 96-well plate and incubated overnight in an incubator at 37°C and 5% CO_2 with 95% humidity. On the following day, the medium was replaced with a medium containing BFNPs or with medium control. Three drug concentrations (100, 50 and 25 μg/mL) were used, and samples at each concentration were ran in sextuplicate. The cells were incubated with BFNPs for 72 h. Wells containing the normal medium without samples were used as the control. The cells were irradiated with 1.5 W cm^{-2} NIR laser (825 nm) for 5 min in photothermal treatment. Briefly, the medium was replaced with cell culture medium containing reagent and incubated for 2 h. Following the incubation, a microplate reader (SpectraMax i3, Molecular Devices, Sunnyvale, CA) was used to determine the fluorescence intensity of the dye (550ex/590em). The fluorescence intensity from cells treated with BFNPs was compared to that from untreated control cells to determine percent viability.

2.10   Histopathological evaluation

Four days after intravenous administration of BFNPs at 0.5 mg/mL, mice were euthanized and whole organs (heart, kidney, liver, lung and spleen) of C57BL/6 mice were removed and preserved in 10% formalin for 48 h. Tissues were then embedded in paraffin, sliced into 5 μm sections, and stained with hematoxylin and eosin. Microscopic images of tissues were acquired using a Nikon ECLIPSE TE2000-S microscope.

2.11   Biodistribution and half-life in blood circulation

Mice with flank xenograft C6 tumors were injected via tail vein with 200 μL of 0.5 mg/mL of BFNPs. Mice receiving no injection were used as controls. Mice were divided into three groups (n = 3 per group). At 24 h, 48 h and 96 h after BFNP injection, animals were euthanized and whole organs of liver, spleen, kidney, lung, heart, and tumor were harvested. Fluorescence was acquired for each tissue type using a Xenogen IVIS imaging system at an excitation wavelength of 640 nm. For assessment of serum half-life of BFNPs, blood was collected from mice at 0.15, 1, 1.5, 2, 2.5, 3, 4, 6, 8, and 10 h after injection of 200 μL of 1

mg/mL of BFNPs. Blood was centrifuged, and plasma was collected. Plasma from mice receiving no BFNPs injection was used to eliminate the background fluorescence. Fluorescence was acquired using a Xenogen IVIS imaging system at an excitation wavelength of 640 nm.

2.12 In vitro PTT

SF-763 cells at a density of 1×10^6 cells per well were incubated for 2 h with PBS solution and BFNPs at a concentration of 1 mg/mL and irradiated with an 825-nm laser at the power density of 1.5 W cm^{-2} for 5 min. The cells were stained with Calcein-AM and propidium iodide (PI) for 15 min, washed with PBS, and then imaged with a confocal fluorescence microscope at an excitation wavelength of 488 nm for cytoplasm and 546 nm for cell nuclei.

2.13 In vivo therapy with BFNPs and NIR irradiation

Flank xenograft C6 tumors were prepared by subcutaneous injection of one million C6 cells suspended in Matrigel (BD Biosciences, San Jose, CA) into the right flanks of athymic nude mice (Jackson Labs, Bar Harbor, ME). Tumors were allowed to grow for 2 weeks. Mice bearing tumors were divided into four groups (n = 4 per group). Two groups were intratumorally injected with 200 μL of PBS with one if two groups subsequently receiving NIR irradiation (825 nm, 1.5 W/cm^2) for 5 min. Another two groups were intratumorally injected with BFNPs (200 μL, 0.5 mg/mL) for two times and then one of the two groups were treated with NIR irradiation (825 nm, 1.5 W/cm^2) for 5 min. Tumor sizes were measured every 2 days for 10 days. The length and width of the tumors were measured with a digital caliper. Ten days after BFNP injection, tumors were harvested for H&E analysis as described in previous section (2.10).

3. Results and discussion

The morphology and structure of BFNPs are examined with transmission electron microscopy (TEM), high-resolution TEM (HRTEM) and selected-area electron diffraction (SAED). Fig. 1a shows that BFNPs are virtually spheroidal and quite uniform in size with an average diameter of about 16 nm. An HRTEM image of a single BFNP (Fig. 1b) reveals the architecture of BFNPs as consisting of a crystalline iron oxide core (9.1 nm in diameter) surrounded by a carbon shell with a thickness of 3.4 nm. Furthermore, Fig. 1c displays the lattice fringes associated with the Fe_3C_4 crystal structure that correspond to the (311) reflections of magnetite. A typical SAED pattern of BFNPs is shown in Fig. 1d showing the diffraction dots which confirm the crystalline nature of BFNPs. X-ray photoelectron spectroscopy (XPS) was used to verify the elemental composition of BFNPs; the results (Fig. S1) show that BFNPs are composed of 58.8% carbon, 33.2% oxygen and 8.0% iron in weight.

The crystallographic structure and phase purity of as-prepared BFNPs were examined by X-ray powder diffraction (XRD) and Raman scattering techniques. The observed reflections of 220, 311, 400, 422, 511 and 440 in the XRD pattern (Fig. 1e) match well with standard magnetite XRD reflections. In the Raman scattering pattern of BFNPs (Fig. 1f), the strong peak at ~1590 cm^{-1} may be assigned to the G band of the carbon shell, while another

dominant peak at ~1387 cm^{-1} may be ascribed to the D band of the carbon shell [35–37]. Additionally, the high-resolution XPS spectrum (Fig. S2) of the C 1 s signal shows oxidized carbon in the form of a carboxylate group at a binding energy of 288.1 eV [38].

The surface properties of BFNPs were further investigated using Fourier transform infrared (FT-IR) spectroscopy (Fig. S3). The FT-IR absorption peak at 1708 cm^{-1} may be attributed to the C=0 stretching band of the carboxylic acid groups conjugated with condensed aromatic carbon, whereas the broad absorption around 3391 cm^{-1} may be assigned to –OH groups [39, 40]. These hydrophilic functional groups facilitates the dispersion of BFNPs in phosphate buffered saline (PBS) solution. BFNPs in PBS have a hydrodynamic diameter of about 27 and a narrow size distribution (Fig. S4a). Furthermore, BFNPs in PBS (Fig. 2a) and in PBS containing 10% serum (Fig. S4b) remained well-dispersed over 7 days and 14 days, respectively, suggesting high-level stability. The UV–Vis absorption spectrum (Fig. 2b) of BFNPs shows a sharp absorption peak at −243 nm which is ascribed to the π-π* transition of aromatic domains in the carbon shell of BFNPs [41, 42]. A shoulder peak at 404 nm is also observed and is attributable to the Fe_3O_4 core of BFNPs [43].

The photoluminescence (PL) properties of BFNPs were studied under different excitation wavelengths (λ_{ex}). As shown in Fig. 2c, when λ_{ex} increases from 240 nm to 500 nm, the emission peak gradually shifts to longer wavelengths and the PL intensity gradually increases, reaches a peak, then decreases. The PL quantum yield of BFNPs was determined to be 5.8 % using rhodamine B as a standard. BFNPs also demonstrate excellent photostability since only a slight change in PL intensity was observed after 2 h continuous exposure of BFNPs in PBS solution to UV excitation light (λ_{ex} = 360 nm) in a fluorospectrometer (Fig. S5). More importantly, the PL spectra (Fig. 2d) of BFNPs excited by long-wavelength light (700 < λ_{ex} < 980) nm clearly demonstrate upconverted emissions from 424 to 530 nm. The tunable PL properties of BFNPs are attributed to the quantum confinement of conjugated π-electrons in sp^2 network and multiphoton active processes within the carbon shell [44, 45].

The magnetic properties of BFNPs were investigated using a superconducting quantum interference device (SQUID) magnetometer. Fig. 2e shows the hysteresis loop of BFNPs measured at 300 K in an applied magnetic field of up to ±20,000 Oe, which indicates that the saturation magnetization (M_s) of BFNPs is 13.6 emu g^{-1}. The value of Ms is relatively low because the BFNPs contain only about 41.22 % of Fe_3O_4, which reduces the relative mass ratio of the magnetic component to the carbon shell in BFNPs may affect the surface property of Fe_3O_4 [46]. No remanence or coercivity was observed at room temperature, which is indicative of the superparamagnetic behavior of BFNPs, an essential for applications in bioseparation, MRI contrast enhancement, and magneto-thermal therapy [47– 49]. An expanded view of the hysteresis loop is displayed in the inset of Fig. 2e showing the resultant magnetization for applied field strengths between −4 and 4 Oe; this plot shows that the coercive force and remaining magnetization saturation is 1.62 Oe and 0.039 emu g^{-1}, respectively. BFNPs show strong NIR absorption (Fig. S6) due to the aromatic, highly π-conjugated carbon structure of their shells, suggesting that BFNPs can serve as phototherapeutic agents inPTT [50, 51]. Fig. 2f shows the photothermal effect of BFNPs upon exposure to an NIR laser irradiation (825 nm) at a power density of 1.5 W/cm^2,

resulting in a concentration- and time-dependent temperature increase. Based on the time constant for heat transfer (Fig. S7) and using the reported method for calculation of the photothermal conversion efficiency (PCE), the PCE of BFNPs can be as high as 20.03%, similar to that reported for gold nanorod (24.4 %) and Fe@Fe_3O_4 NPs (20.3 %) [16, 24]. In comparison, the temperature change of water, used as a control, was much less significant under the same irradiation condition.

Due to the fact that BFNPs consist of both fluorescent carbon shells and superparamagnetic Fe_3O_4 cores, these particles should provide dual-modal imaging capabilities for FL bioimaging and MRI. Human SF-763 glioblastoma cells were used to evaluate the FL imaging functionality of BFNPs in vitro. Fig. 3 a-c show laser scanning confocal images of SF-763 cells incubated with BFNPs acquired at different excitation wavelengths (405, 488, and 546 nm). BFNPs produced a bright FL signal and illuminated SF-763 cells. A comparison of confocal images (Fig. S8) of SF-763 cells incubated with PBS solution further confirms that such optical property was generated by BFNPs. Additionally, the confocal FL signal did not decrease after continuous irradiation with λ_{ex} = 488 nm for 60 min (Fig. S9), suggesting that BFNPs have excellent photo stability and can be used for long-term cellular imaging. BFNPs were primarily localized in the cytoplasm of SF-763 cells and did not appear in cell nuclei. This indicates that BFNPs could potentially be used as a phototherapeutic agent capable of infiltrating the cell membrane of cancerous cells which would be advantageous in PTT.

Given the observed PL upconversion properties of BFNPs (Fig. 2d), these particles are expected to serve as convenient optical marker in two-photon FL imaging. Fig. 3d-f shows a transmission image (d), a two-photon FL image (e) and their overlay (f) of SF-763 cells after up taking BFNPs and being excited with a femtosecond infrared laser (λ_{ex} = 820 nm). These images show that cell structures may be highlighted using the upconverted FL signal emitted by BFNPs upon excitation with an NIR laser irradiation. NIR imaging with BFNPs was further investigated in vivo by injecting BFNPs into flank tumors of mice. As shown in Fig. 3 g-j and k-n the FL signal of BFNPs injected into a tumor (dose = 10 mg kg^{-1}) and BFNPs in PBS solution at excitation wavelengths of 605, 640 and 675 nm using an in vivo imaging system (IVIS) was observed.

The superparamagnetism exhibited by BFNPs indicates their ability to serve as T_2 contrast agents for MRI; this was tested in vitro using a quantitative T_2 imaging sequence to determine the transverse relaxivity rate (r_2) of BFNPs. Fig. 4a shows the inverse relaxation times (1 /T_2) of BFNPs as a function of iron concentration. The transverse relaxivity of the BFNPs was found to exhibit a linear relationship with iron concentration, with r_2 = 264.76 mM^{-1} s^{-1}, an r_2 which is much greater than those of commonly used clinical T_2 contrast agents (e.g., Feridex, r_2 = 185.84 mM^{-1} s^{-1}, Fig. S10). T_2-weighted magnetic resonance images and R_2 maps (Fig. 4b) reveal that the T_2 MRI signal intensity declines with increasing BFNP concentration; the reason for this is that magnetic Fe_3O_4 cores shorten the transverse relaxation time (i.e., T_2) by dephasing the spins of protons in their vicinity [52]. The incremental decrease in MRI signal intensity is indicated by the enhanced darkness at increased iron concentrations. To evaluate their MR imaging capability in vivo, BFNPs (1 mg/mL, 200 μL) were administered through intravenous injection. T_2-weighted MR images

of the cross-section views of mice centered on kidney and spleen were acquired before and after the injection (Fig. 4c). BFNPs demonstrated a substantial contrast enhancement throughout the duration of the experiment (60 min). These results show the ability of the BFNPs to serve as contrast agents in T_2-weighted MRI for diagnosis and monitoring treatment of cancer.

The in vitro cytotoxicities of BFNPs with and without NIR irradiation were evaluated using a glioma cell line (SF-763) and a healthy cell line (HEK293T). Fig. 5a and b show the cytotoxicity of BFNPs at various concentrations with and without 5 min exposure to 1.5 W/cm^2 NIR light. More than 95% of cells from both cell lines survived 72 h after treatment with BFNPs without NIR irradiation, which indicates that BFNPs are nontoxic to the tested cells at concentrations up to 100 μg mL^{-1}. However, laser irradiation led to a significant decrease in cell viability, down to 58%, after cells were incubated with 100 μg mL^{-1} of BFNPs. Conversely, exposing cells alone (i.e., cells not incubated with BFNPs) to NIR laser irradiation showed a negligible effect on their cell viability (Fig. S11). Confocal fluorescent images of calcein AM (green, live cells) and propidium iodide (PI) (red, dead cells) co-stained cells shown the death of the SF-763 cells after incubation with BFNPs while no cell death was observed in SF-763 cells after incubation with PBS solution (Fig. S12), which further confirmed the effective photothermal therapy induced by BFNPs (Fig. 5d). These results show the great potential of BFNPs to serve as phototherapeutic agents in PTT.

The biodistribution and tissue toxicity of BFNPs were assessed in vivo. An experimental group and a control group of mice with a tumor were intravenously injected with BFNPs (dose =200 μL, 1 mg mL^{-1}) and PBS (volume = 200 μL), respectively. Mice were then euthanized and whole organs, including liver, spleen, kidney, lung, heart, and tumor were harvested at different time points. BFNP biodistribution was assessed by measuring the FL signal of BFNPs using an IVIS system at an excitation wavelength of 640 nm. As shown in Fig. 5c, BFNPs mainly accumulated in the liver due to reticuloendothelial system uptake; BFNPs were also found in the kidneys, spleen, lungs, heart, and tumor in order from highest concentration to lowest. At 96 h post-injection, less than 15% of initially-accumulated BFNPs remained in the liver and minimal amounts of BFNPs were found in the heart, kidneys, lungs and spleen. Histological analysis of the major organs was performed to evaluate the tisssue toxicity of BFNPs. Tissues were harvested from mice 96 h after BFNP injection; tissues were then fixed in 10% formalin, embedded in paraffin, sectioned and stained with hematoxylin and eosin (H & E). As shown in Fig. 5e, no discernible differences in cell morphology or tissue structure were observed between treated mice and control mice, suggesting that BFNPs are non-toxic to healthy tissues. In addition, the half-life of BFNPs in blood circulation was found to be 1.36 h (Fig. S13)

Given their demonstrated photothermal conversion efficiency and non-toxic property? [?]good compatibility, BFNPs were assessed in a preliminary in vivo PTT study. Mice bearing C6 glioblastoma tumors were allowed to grow for 2 weeks before being administrated with BFNPs via a single intratumoral injection and the tumor regions were then subjected or not subjected to NIR laser irradiation (825 nm, 1.5 W/cm^2) for 5 min in experimental and control conditions, respectively. Tumor-bearing mice were randomly divided into 4 groups with 4 mice per group. Two groups were intratumorally injected with

PBS solution, where one group received NIR laser irradiation and the other did not. The mice in the other two groups were intratumorally injected with BFNPs, where one group received NIR laser irradiation and the other did not. Tumor sizes in mice were measured every two days up to 10 days post-treatment. As shown in Fig. 6a, the tumors in both PBS-injected groups grew rapidly, regardless of NIR irradiation. The tumors in mice treated with BFNPs but not NIR laser irradiation exhibited similar tumor growth profiles compared to both PBS-treated groups. For these three groups, the tumors grew steadily, with tumor sizes increasing 7-fold relative to the initial tumor size. In contrast, a remarkable inhibition of tumor growth was observed in mice treated with both BFNPs and NIR laser irradiation. The weight of all mice in each group was also recorded; Fig. 6b displays the average weight for all the mice in a group for all 4 groups over a 10-day period. The weight of all mice in all groups remained in a normal range and no obvious weight loss or gain was observed. At day 10, tumors from all mice were harvested and weighed. The average tumor mass from the group treated with both BFNP and NIR laser irradiation was significantly smaller than those from the other three groups (Fig. S14). To further elucidate the effects of PTT on tumor regions, tumor tissues were harvested from mice after treatment (i.e., day 10). Histological images of H&E stained tumor sections (Fig. 6c) show that cells in tumors from mouse groups treated with PBS, PBS + NIR irradiation and BFNP alone largely retained their normal cancerous morphology with distinctive membranes and nuclear structures. On the contrary, most tumor cells from the group treated with BFNPs and NIR irradiation were severely damaged and exhibited shrinkage, loss of contact and nuclear damage. These results suggest that BFNPs could serve as effective phototherapeutic agents for in vivo PTT of cancer.

4 Conclusions

Theranostic hybrid nanostructures based on Fe_3O_4 nanocrystal cores with carbon shells were synthesized using a one-pot solvothermal method with ferrocene as the sole precursor. The resultant BFNPs have a uniform size of about 16 nm and excellent stability in solution due to the presence of hydrophilic carboxyl groups on the surface of carbon shell. The carbon shell in BFNPs exhibits excitation wavelength-tunable photoluminescence, which allow BFNPs to serve as an optical maker for confocal, two-photon fluorescence and NIR imaging. f The Fe_3O_4 cores in BFNPs are superparamagnetic in nature, which provides contrast enhancement for T_2-weighted MRI in vivo. Both in vitro and in vivo studies show that the BFNPs are non-toxic to cells and healthy tissues. Also notably, BFNPs can absorb and convert NIR light to heat and thus, can enable photothermal therapy for tumor treatment. With multiple favorable functionalities, this nanostructure holds great promise to improve the outcome in imaging-guided cancer therapy.

Supplementary Material

Refer to Web version on PubMed Central for supplementary material.

Acknowledgements

Notes and references

[1]. Cheng L, Wang C, Feng L, Yang K, Liu Z, Functional Nanomaterials for Phototherapies of Cancer, Chemical Reviews, 114 (2014) 10869–10939. [PubMed: 25260098]

[2]. Abadeer NS, Murphy CJ, Recent Progress in Cancer Thermal Therapy Using Gold Nanoparticles, The Journal of Physical Chemistry C, 120(2016) 4691–4716.

[3]. Shibu ES, Hamada M, Murase N, Biju V, Nanomaterials formulations for photothermal and photodynamic therapy of cancer, Journal of Photochemistry and Photobiology C: Photochemistry Reviews, 15 (2013) 53–72.

[4]. Jaque D, Martinez Maestro L, del Rosal B, Haro-Gonzalez P, Benayas A, Plaza JL, Martin Rodriguez E, Garcia Sole J, Nanoparticles for photothermal therapies, Nanoscale, 6 (2014) 9494–9530. [PubMed: 25030381]

[5]. Chen Q, Xu L, Liang C, Wang C, Peng R Liu Z, Photothermal therapy with immune-adjuvant nanoparticles together with checkpoint blockade for effective cancer immunotherapy, Nature Communications, 7(2016) 13193.

[6]. Wang H Wang K Mu Q, Stephen ZR, Yu Y, Zhou S, Zhang M Mesoporous carbon nanoshells for high hydrophobic drug loading, multimodal optical imaging, controlled drug release, and synergistic therapy, Nanoscale, 9 (2017) 1434–1442. [PubMed: 28094402]

[7]. Zou L, Wang H, He B, Zeng L Tan T, Cao H, He X, Zhang Z, Guo S, Li Y, Current Approaches of Photothermal Therapy in Treating Cancer Metastasis with Nanotherapeutics, Theranostics, 6(2016) 762–772. [PubMed: 27162548]

[8]. Wang H, Mukherjee S, Yi J, Baneijee P, Chen Q, Zhou S, Biocompatible Chitosan-Carbon Dots Hybrid Nanogels for NIR-Imaging-Guided Synergistic Photothermal/Chemo-Therapy, ACS Applied Materials & Interfaces, (2017).

[9]. Zhang M Cao Y, Wang L Ma Y, Tu X, Zhang Z Manganese Doped Iron Oxide Theranostic Nanoparticles for Combined T1 Magnetic Resonance Imaging and Photothermal Therapy, ACS Applied Materials & Interfaces, 7 (2015) 4650–4658. [PubMed: 25672225]

[10]. Liu Y, Guo Q, Zhu X, Feng W Wang L Ma L, Zhang G Zhou J, Li F, Optimization of Prussian Blue Coated NaDyF4:x%Lu Nanocomposites for Multifunctional Imaging-Guided Photothermal Therapy, Advanced Functional Materials, 26 (2016) 5120–5130.

[11]. Wang D Zhou J, Chen R, Shi R, Zhao G, Xia G, Li R, Liu Z, Tian J, Wang H Guo Z, Wang H Chen Q, Controllable synthesis of dual-MOFs nanostructures for pH-responsive artemisinin delivery, magnetic resonance and optical dual-model imaging-guided chemo/photothermal combinational cancer therapy, Biomaterials, 100 (2016)27–40. [PubMed: 27240160]

[12]. Wang H Sun Y, Yi J, Fu J, Di J, del Carmen Alonso A, Zhou S, Fluorescent porous carbon nanocapsules for two-photon imaging NIR/pH dual-responsive drug carrier, and photothermal therapy, Biomaterials, 53 (2015) 117–126. [PubMed: 25890712]

[13]. Wang D Guo Z, Zhou J, Chen J, Zhao G, Chen R, He M, Liu Z, Wang H Chen Q, Novel Mn3[Co(CN)6]2@SiO2@Ag Core–Shell Nanocube: Enhanced Two-Photon Fluorescence and Magnetic Resonance Dual-Modal Imaging-Guided Photothermal and Chemo-therapy, Small, 11 (2015)5956–5967. [PubMed: 26437078]

[14]. Xia Y, Li W, Cobley CM, Chen J, Xia X, Zhang Q Yang M Cho EC, Brown PK, Gold Nanocages: From Synthesis to Theranostic Applications, Acc. Chem. Res, 44 (2011) 914–924. [PubMed: 21528889]

[15]. Wang H Cao G, Gai Z, Hong K Baneijee P, Zhou S, Magnetic/NIR-responsive drug carrier, multicolor cell imaging and enhanced photothermal therapy of gold capped magnetite-fluorescent carbon hybrid nanoparticles, Nanoscale, 7(2015)7885–7895. [PubMed: 25854197]

[16]. Tian Q, Jiang F Zou R, Liu Q, Chen Z, Zhu M, Yang S Wang J Wang J Hu J, Hydrophilic Cu9S5 Nanocrystals: A Photothermal Agent with a 25.7% Heat Conversion Efficiency for Photothermal Ablation of Cancer Cells in Vivo, ACS Nano, 5 (2011) 9761–9771. [PubMed: 22059851]

[17]. Chou SS, Kaehr B, Kim J, Foley BM, De M, Hopkins PE, Huang J Blinker CJ, Dravid VP, Chemically Exfoliated MoS2 as Near-Infrared Photothermal Agents, Angew. Chem. Int. Ed, 52 (2013) 4160–4164.

[18]. Liu T, Wang C Gu X, Gong H Cheng L Shi X, Feng L Sun B, Liu Z, Drug Delivery with PEGylated MoS2 Nano-sheets for Combined Photothermal and Chemotherapy of Cancer, Adv. Mater, 26 (2014) 3433–3440. [PubMed: 24677423]

[19]. Zou L, Wang H He B, Zeng L Tan T, Cao H, He X, Zhang Z Guo S, Li Y, Current Approaches of Photothermal Therapy in Treating Cancer Metastasis with Nanotherapeutics, Theranostics, 6(2016) 762–772. [PubMed: 27162548]

[20]. Lovell JF, Jin CS, Huynh E, Jin H, Kim C, Rubinstein JL, Chan WCW, Cao W, Wang LV Zheng G Porphysome nanovesicles generated by porphyrin bilayers for use as multimodal biophotonic contrast agents, Nat Mater, 10 (2011) 324–332. [PubMed: 21423187]

[21]. Cheng L, He W, Gong H, Wang C Chen Q, Cheng Z Liu Z, PEGylated Micelle Nanoparticles Encapsulating aNon-Fluorescent Near-Infrared Organic Dye as a Safe and Highly-Effective Photothermal Agent for In Vivo Cancer Therapy, Adv. Funct. Mater, 23 (2013) 5893–5902.

[22]. Wang H Wang K Tian B, Revia R, Mu Q, Jeon M, Chang F-C Zhang M Preloading of Hydrophobic Anticancer Drug into Multifunctional Nanocarrier for Multimodal Imaging NIR-Responsive Drug Release, and Synergistic Therapy, Small, 12 (2016)6388–6397. [PubMed: 27671114]

[23]. Song X Chen Q, Liu Z, Recent advances in the development of organic photothermal nano-agents, Nano Research, 8 (2015) 340–354.

[24]. Zhou Z, Sun Y, Shen J, Wei J, Yu C, Kong B Liu W, Yang H Yang S Wang W Iron/iron oxide core/shell nanoparticles for magnetic targeting MRI and near-infrared photothermal therapy, Biomaterials, 35 (2014) 7470–7478. [PubMed: 24881997]

[25]. Jeong CJ Sharker SM, In I, Park SY, Iron Oxide@PEDOT-Based Recyclable Photothermal Nanoparticles with Poly(vinylpyrrolidone) Sulfobetaines for Rapid and Effective Antibacterial Activity, ACS Applied Materials & Interfaces, 7 (2015) 9469–9478. [PubMed: 25905634]

[26]. Ge J, Jia Q, Liu W, Guo L, Liu Q, Lan M, Zhang H Meng X Wang PRed-Emissive Carbon Dots for Fluorescent, Photoacoustic, and Thermal Theranostics in Living Mice, Adv. Mater, 27 (2015) 4169–4177. [PubMed: 26045099]

[27]. Cheng L Yang K Chen Q, Liu Z, Organic Stealth Nanoparticles for Highly Effective in Vivo Near-Infrared Photothermal Therapy of Cancer, ACS Nano, 6(2012) 5605–5613. [PubMed: 22616847]

[28]. Bao Z, Liu X, Liu Y, Liu H, Zhao K, Near-infrared light-responsive inorganic nanomaterials for photothermal therapy, Asian Journal of Pharmaceutical Sciences, 11 (2016) 349–364.

[29]. Chen Q, Wen J, Li H, Xu Y, Liu F, Sun S, Recent advances in different modal imaging-guided photothermal therapy, Biomaterials, 106 (2016) 144–166. [PubMed: 27561885]

[30]. Veiseh O, Gunn JW, Zhang M Design and fabrication of magnetic nanoparticles for targeted drug delivery and imaging Adv. Drug Del. Rev, 62 (2010) 284–304.

[31]. Revia RA, Zhang M Magnetite nanoparticles for cancer diagnosis, treatment, and treatment monitoring: recent advances, Mater. Today, 19 (2016) 157–168.

[32]. Wang H Revia R, Wang K Kant RJ, Mu Q, Gai Z, Hong K Zhang M Paramagnetic Properties of Metal-Free Boron-Doped Graphene Quantum Dots and Their Application for Safe Magnetic Resonance Imaging Adv Mater, 29 (2017).

[33]. Shimmer W, Pichlmeier U, Meinel T, Wiestler OD, Zanella F, Reulen H-J, Fluorescence-guided surgery with 5-aminolevulinic acid for resection of malignant glioma: a randomised controlled multicentre phase III trial, The Lancet Oncology, 7 392–401. [PubMed: 16648043]

[34]. Wang H Shen J, Li Y, Wei Z, Cao G, Gai Z, Hong K Banerjee P, Zhou S, Magnetic iron oxide-fluorescent carbon dots integrated nanoparticles for dual-modal imaging near-infrared light-responsive drug carrier and photothermal therapy, Biomaterials Science, 2(2014)915.

[35]. Ferrari AC, Robertson J, Interpretation of Raman spectra of disordered and amorphous carbon, Physical Review B, 61 (2000) 14095–14107.

[36]. Ristein J, Stief RT, Ley L, Beyer W, A comparative analysis of a-C:H by infrared spectroscopy and mass selected thermal effusion, J. Appl. Phys, 84 (1998) 3836–3847.

[37]. Wang H Chen Q-W, Sun Y-B, He M-Y, Synthesis of Superparamagnetic Colloidal Nanochains as Magnetic-Responsive Bragg Reflectors, The Journal of Physical Chemistry C, 114 (2010) 19660–19666.

[38]. Kim IT, Nunnery GA, Jacob K, Schwartz J, Liu X, Tannenbaum R, Synthesis, Characterization, and Alignment of Magnetic Carbon Nanotubes Tethered with Maghemite Nanoparticles, The Journal of Physical Chemistry C, 114 (2010) 6944–6951.

[39]. Duffy P, Magno LM, Yadav RB, Roberts SK, Ward AD, Botchway SW, Colavita PE, Quinn SJ, Incandescent porous carbon microspheres to light up cells: solution phenomena and cellular uptake, J. Mater. Chem, 22 (2012) 432–439.

[40]. Wang H, Shen J, Li Y, Wei Z, Cao G, Gai Z, Hong K, Banerjee P, Zhou S, Porous carbon protected magnetite and silver hybrid nanoparticles: morphological control, recyclable catalysts, and multicolor cell imaging, ACS Appl Mater Interfaces, 5 (2013) 9446–9453. [PubMed: 24001139]

[41]. Chang Y-R, Lee H-Y, Chen K, Chang C-C, Tsai D-S, Fu C-C, Lim T-S, Tzeng Y-K, Fang C-Y, Han C-C, Chang H-C, Fann W, Mass production and dynamic imaging of fluorescent nanodiamonds, Nat Nano, 3 (2008) 284–288.

[42]. Wang H, Zhuang J, Velado D, Wei Z, Matsui H, Zhou S, Near-Infrared- and Visible-Light-Enhanced Metal-Free Catalytic Degradation of Organic Pollutants over Carbon-Dot-Based Carbocatalysts Synthesized from Biomass, ACS Appl Mater Interfaces, 7 (2015) 27703–27712. [PubMed: 26615668]

[43]. Martin M, Salazar P, Villalonga R, Campuzano S, Pingarron JM, Gonzalez-Mora JL, Preparation of core-shell Fe3O4@poly(dopamine) magnetic nanoparticles for biosensor construction, Journal of Materials Chemistry B, 2 (2014) 739–746.

[44]. Lee E, Ryu J, Jang J, Fabrication of graphene quantum dots via size-selective precipitation and their application in upconversion-based DSSCs, Chem. Commun, 49 (2013) 9995–9997.

[45]. Eda G, Lin Y-Y, Mattevi C, Yamaguchi H, Chen H-A, Chen IS, Chen C-W, Chhowalla M, Blue Photoluminescence from Chemically Derived Graphene Oxide, Adv. Mater, 22 (2010) 505–509. [PubMed: 20217743]

[46]. Wang H, Yi J, Mukherjee S, Banerjee P, Zhou S, Magnetic/NIR-thermally responsive hybrid nanogels for optical temperature sensing, tumor cell imaging and triggered drug release, Nanoscale, 6 (2014)13001–13011. [PubMed: 25243783]

[47]. Wei W, Zhaohui W, Taekyung Y, Changzhong J, Woo-Sik K, Recent progress on magnetic iron oxide nanoparticles: synthesis, surface functional strategies and biomedical applications, Science and Technology of Advanced Materials, 16 (2015) 023501. [PubMed: 27877761]

[48]. Liu F, Laurent S, Fattahi H, Elst LV, Muller RN, Superparamagnetic nanosystems based on iron oxide nanoparticles for biomedical imaging, Nanomedicine, 6 (2011) 519–528. [PubMed: 21542689]

[49]. Laurent S, Saei AA, Behzadi S, Panahifar A, Mahmoudi M, Superparamagnetic iron oxide nanoparticles for delivery of therapeutic agents: opportunities and challenges, Expert Opinion on Drug Delivery, 11 (2014) 1449–1470. [PubMed: 24870351]

[50]. Yang K, Zhang S, Zhang G, Sun X, Lee S-T, Liu Z, Graphene in Mice: Ultrahigh In Vivo Tumor Uptake and Efficient Photothermal Therapy, Nano Lett, 10 (2010) 3318–3323. [PubMed: 20684528]

[51]. Wang H, Di J, Sun Y, Fu J, Wei Z, Matsui H, Alonso A. del C., Zhou S, Biocompatible PEG-Chitosan@Carbon Dots Hybrid Nanogels for Two-Photon Fluorescence Imaging, Near-Infrared Light/pH Dual-Responsive Drug Carrier, and Synergistic Therapy, Adv. Funct. Mater, 25 (2015) 5537–5547.

[52]. Nasongkla N, Bey E, Ren J, Ai H, Khemtong C, Guthi JS, Chin S-F, Sherry AD, Boothman DA, Gao J, Multifunctional Polymeric Micelles as Cancer-Targeted, MRI-Ultrasensitive Drug Delivery Systems, Nano Lett, 6 (2006) 2427–2430. [PubMed: 17090068]

Highlights

- A bifunctional theranostic nanoparticle (BFNP) is developed.

- BFNP is a contrast agent for both magnetic resonance imaging and fluorescence imaging

- BFNP converts NIR light into heat enabling photothermal therapy

- BFNP is benign to organs and healthy tissue

- Imaging and therapeutic efficacy of BFNP is demonstrated in a mouse model
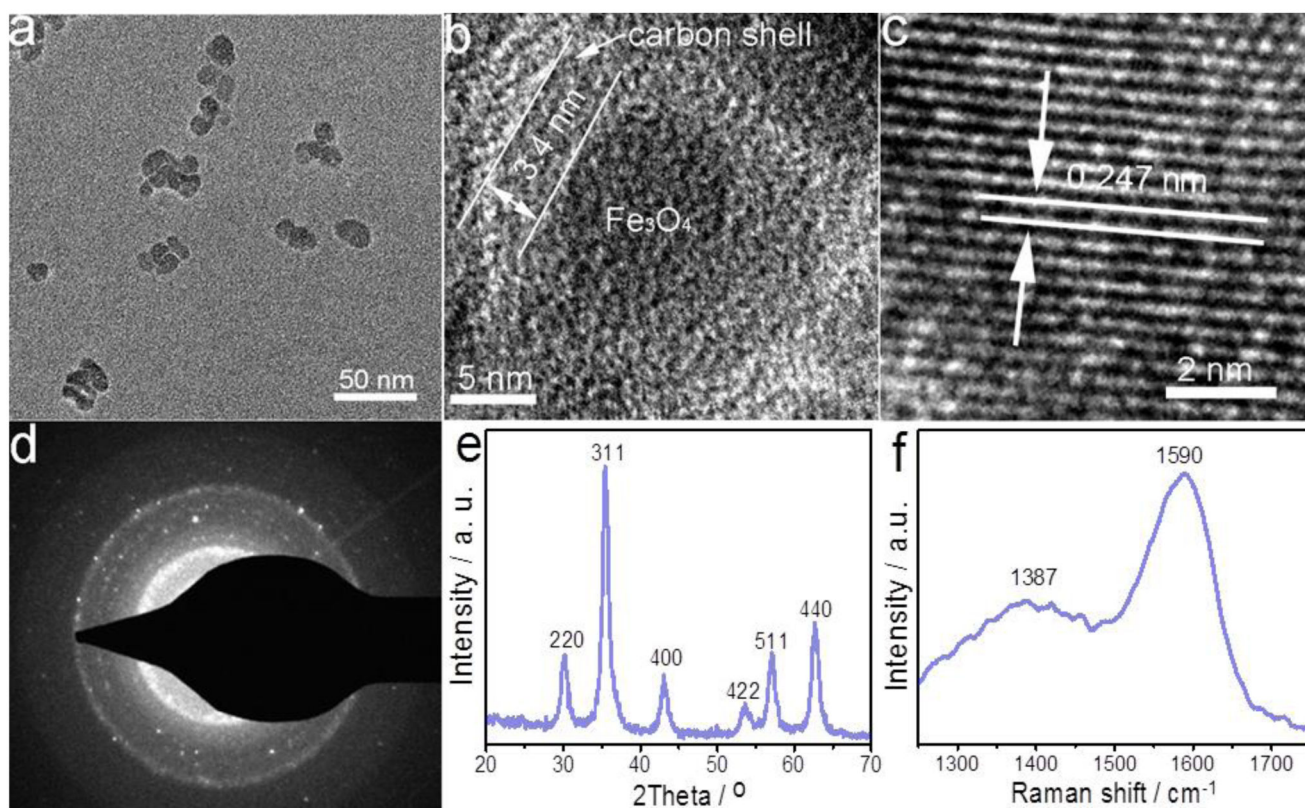
Fig.1.

Morphology and structure of BFNPs. (a) TEM image of BFNPs. (b) HRTEM image of a single BFNP. (c) Lattice fringes of Fe_3O_4 core, (d) SAED pattern of a single BFNP. (e and f) XRD and Raman spectrum of BFNPs, respectively.

Fig. 2.

Characterization of BFNPs. (a) Hydrodynamic size of BFNPs as a function of time. The low variation in hydrodynamic size versus time suggests good stability, (b) UV-Vis-NIR absorption spectrum of BFNPs. (c) PL spectra and (d) upconverted PL spectra of BFNPs under different excitation wavelengths, (e) Hysteresis loop of BFNPs measured at room temperature. The top-left inset shows the respective expanded plots for fields between −4 and 4 Oe. (f) Photothermal heating curves of pure water (control) and BFNPs (0.1, 0.3 and 0.5 mg/mL) in water under 825 nm laser irradiation at a power of 1.5 W/cm^2 for 5 min.
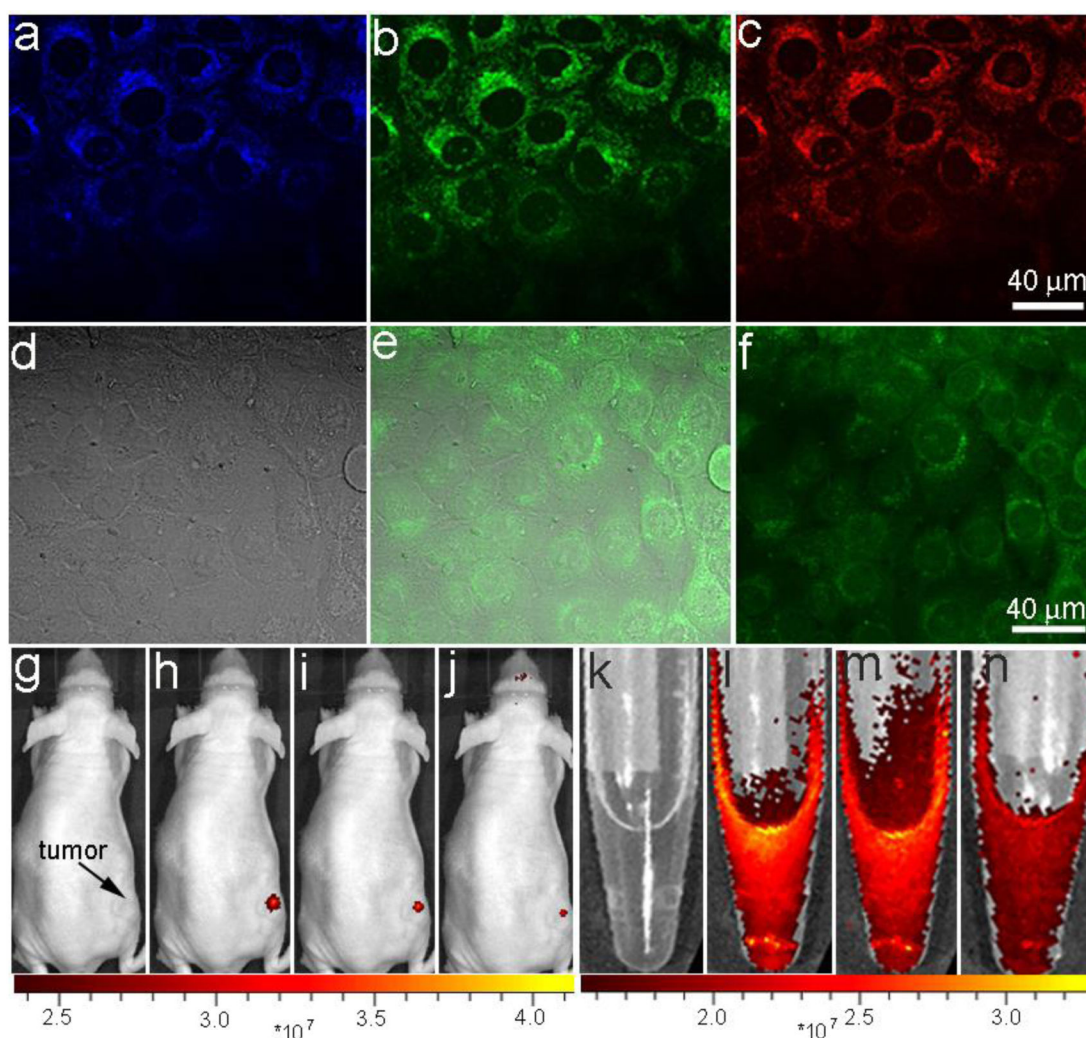
Fig. 3.
In vitro and in vivo FL imaging. Laser scanning confocal microscopy images of SF-763 cells incubated with BFNPs for 2 h under different excitation wavelengths: (a) 405 nm; (b) 488 nm; (c) 546 nm. (d) Transmission, (e) two-photon fluorescence and (f) overlaid images of SF-763 cells incubated with BFNPs. Excitation laser wavelength was 820 nm. NIR FL images of BFNPs injected into a tumor (g-j) and BFNPs (k-n) in PBS solution (0.5 mg/mL, inset) under various excitation wavelengths: (g and k) white light, (h and l) 605 nm, (i and m) 640 nm and (j and n) 675 nm.
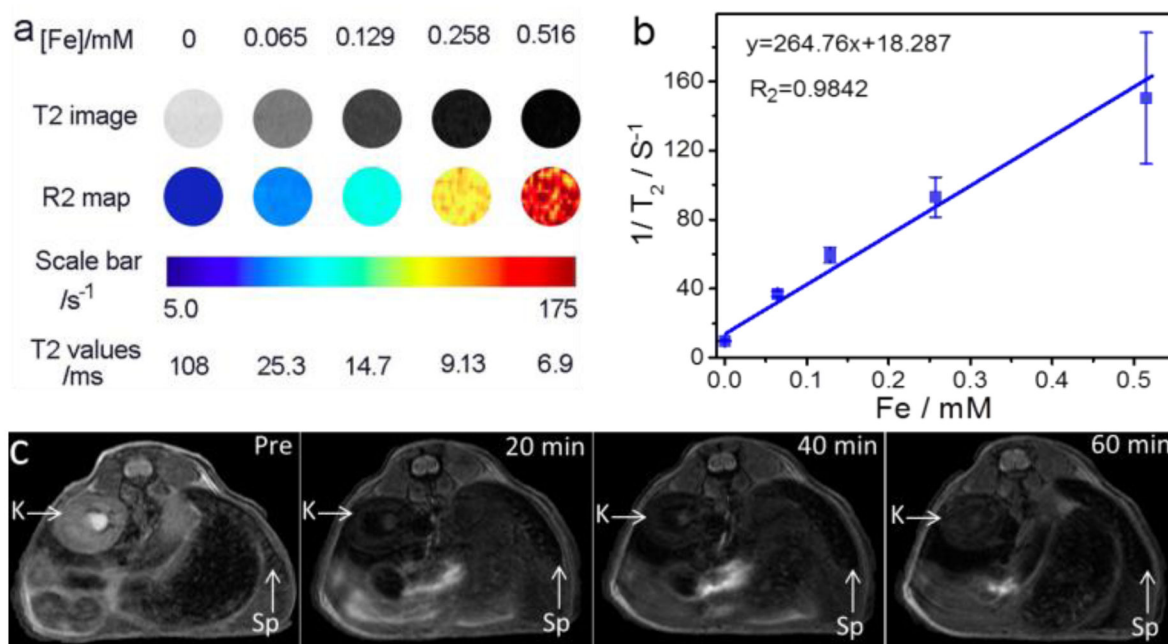
Fig. 4.
MRI of BFNPs. (a) T_2-weighted MR images and R_2 maps of MRI phantoms for BFNPs at different iron concentrations, (b) Plots of l/T_2 as a function of iron concentration. The slope of the curve in (b) is defined as the transverse relaxivity, r_2. (c) In vivo T_2-weighted MR images of the cross-sections of mice receiving BFNPs treatment with dynamic time-resolved MRI acquired at various time points after intravenous administration. The arrows denote various organs: kidney (K) and spleen (Sp).
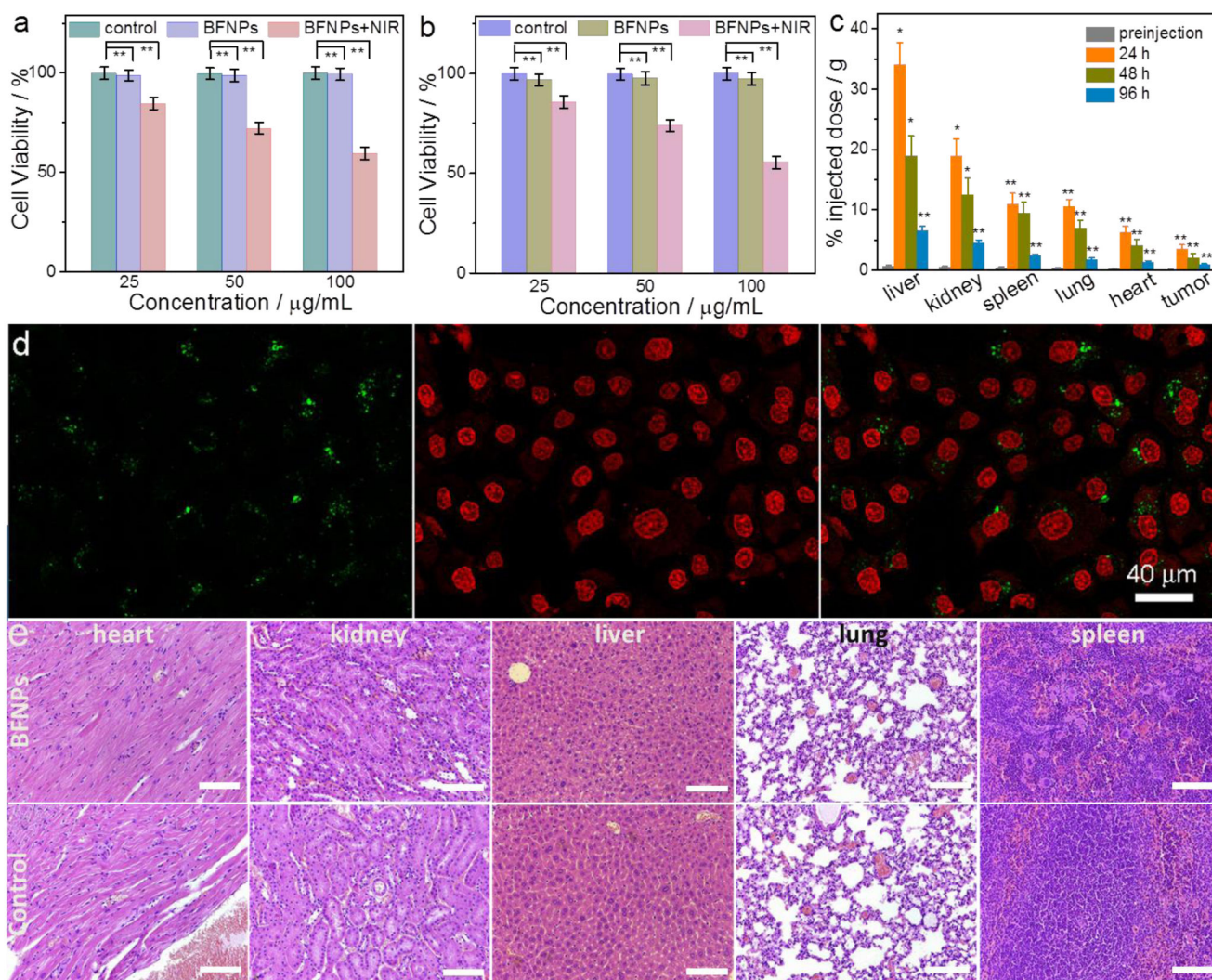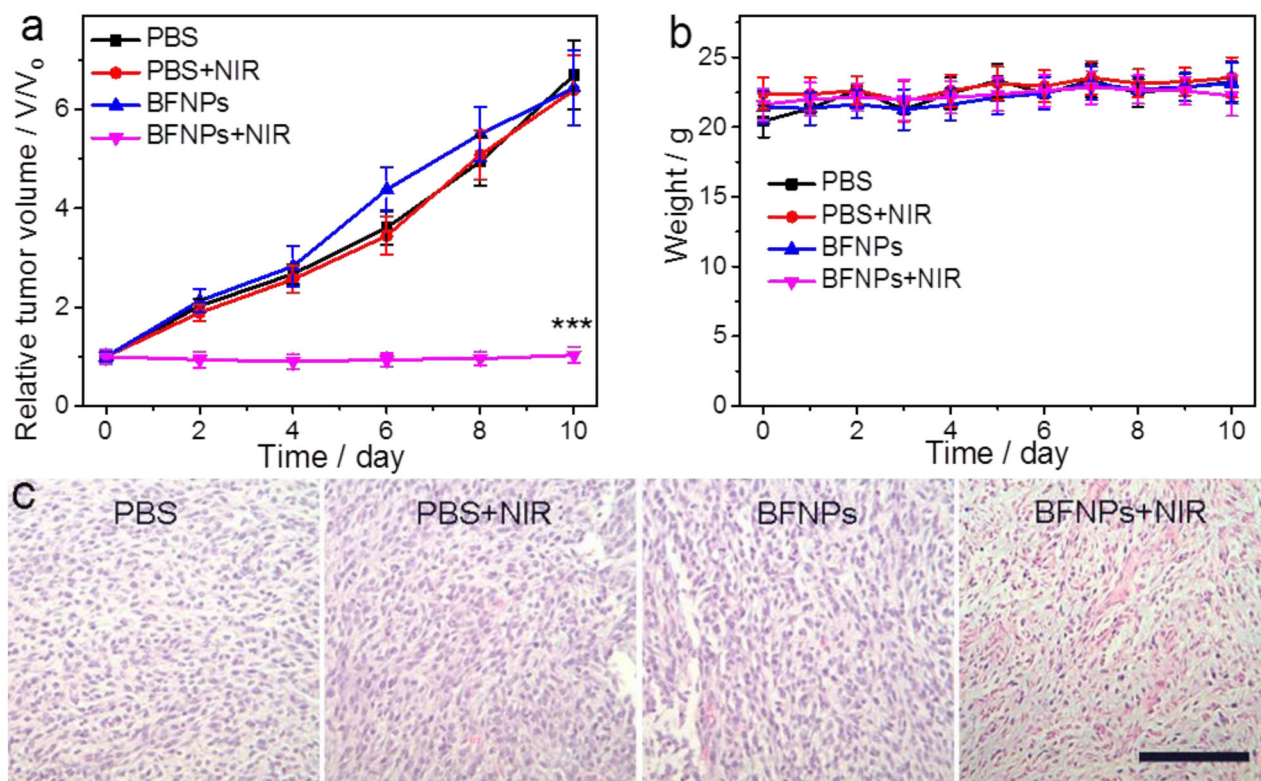
Fig. 5.

Cytotoxicy and tissue toxicity of BFNPs. In vitro cytotoxicity study of BFNPs was performed by assessing the viability of (a) SF-763 and (b) HEK293T cells with and without 5 min exposure to 1.5 W/cm^2 NIR light (825 nm). (c) Biodistribution of BFNPs in different organs of nude mice evaluated at 24 h, 48 h and 96 h post-injection, (d) Confocal images of calcein AM (green, live cells) and propidium iodide (red, dead cells) co-stained stained SF-763 cells (left, cytoplasm; middle, cell nucleus; right, overlaid images) after incubation with BFNPs and being exposed to the 825 nm laser at the power density of 1.5 W cm^{-2} for 5 min. (e) Histological images of H & E stained tissue sections of mouse heart, kidney, liver, lung and spleen obtained from non-injected animals (control) and those injected with BFNPs at a concentration of 1 mg mL^{-1}. The scale bar is 100 μm. Data in (a) are presented in mean ± SEM (n= 6). Statistical analysis was performed using the Student's two-tailed t-test with $*$ $p < 0.05$ and $**$ $p < 0.01$ considered as statistically significant.

Fig. 6.

In vivo PTT using BFNPs. (a) Tumor growth curves of mice treated under different conditions (four mice per treatment group). (b) Weight of mice from different groups over a 10-day period, (c) H & E-stained tumor sections collected from mice after treatments (scale bar =125 μm). Statistical analysis was performed using the Student's two-tailed *T*-test (***P< 0.001).